Impact of structural uncertainty on tracer test design in faulted geothermal reservoirs

Ali Dashti [a,*], Maziar Gholami Korzani [a,b], Christophe Geuzaine [c], Robert Egert [a], Thomas Kohl [a]

[a] Institute of Applied Geosciences, Karlsruhe Institute of Technology (KIT), Karlsruhe, Germany
[b] School of Civil and Environmental Engineering, Queensland University of Technology, Brisbane, Australia
[c] Université de Liège, Institut Montefiore B28, Liège 4000, Belgium

ARTICLE INFO

Keywords:
Uncertainty quantification
Structural uncertainty
Geothermal reservoir
Probabilistic models

ABSTRACT

Evaluation of underground processes requires numerical modeling based on sophisticated and reliable meshing. Our new *GeoMeshPy* library focuses on the discretization of probabilistic geological structures. This study presents a synthetic show-case for the capacity of this library to quantify the impact of structural uncertainty. In here, 50 models were developed taking advantage of the computational efficiency of *GeoMeshPy*. Assuming a geothermal doublet system embedded in a faulted reservoir with unclear structure, recovery time and magnitude of a tracer breakthrough was calculated. Even small angular variations up to ±15° in one of the faults yield differences of up to 26 and 30 percent for peak arrival time and magnitude, respectively. An additional inversion scheme of each of the 50 curves allows quantifying the impact on Péclet number varying from 3.4 to 4.3 due to structural variability. Analytically calculated dispersion coefficients are almost one order of magnitude higher than values used for simulations. Besides this mismatch, calculated dispersion coefficients are unable to represent the structural uncertainty (ranging from 125.6 to 129.4 m).

1. Introduction

An understanding of the underground flow regime is a pivotal necessity for any long-term subsurface application. Flow characterization through tracer tests is vital in a wide variety of reservoir engineering. Applications are in the fields of geothermal (Malik et al., 2020; Sanjuan et al., 2006), conventional hydrocarbons (Li et al., 2019; Lu et al., 2012), shale gas (Middleton et al., 2015), CO_2 storage (Flohr et al., 2021; Jenkins et al., 2015), nuclear or toxic waste disposals (Hadgu et al., 2017; Klein et al., 2021) and so on. For safety issues, these tests are of high importance since they provide a robust underground knowledge in field scale. Furthermore, legal regulations necessitate a reliable forecasting system on a millennial timescale e.g. for CO_2 storage. Success of such projects (CO_2 storage) hinges on various interconnected factors (Al-Khdheeawi et al., 2017; Fauziah et al., 2020) but adding the underground geometry makes the assessment more integrated and reliable.

Since fluid flow in fractures typically dominates the total regime (Cao et al., 2019; Siler and Pepin, 2021; Zhang et al., 2019), characterization of these zones is crucial for designing exploitation concepts (Tsang et al., 1996). However, the bias between structural information and flow regime can lead to oversimplifications for reservoir production scheme. Even in permeable fractures the nature of flow is a problematic and active subject matter (Cox, 2020; Egert et al., 2021; Fairley and Hinds, 2004; Phillips et al., 2020).

To quantify the influence of faults on the performance of the reservoir, detailed understanding about their geometry is essential but rarely available (Konrad et al., 2021). Depending on the experience of the interpreter, faults are detected from visually recognizable lineaments of discontinuities in reflection patterns on 2/3D seismic data. Besides the interpretation uncertainty, variations of wave velocity or acquisition quality can introduce errors in the structural definition of a fault system (Faleide et al., 2021; Michie et al., 2021; Røe et al., 2014). This may even apply to state-of-the-art fault detection methods deploying automated machine learning algorithms (Al-Maskeen et al., 2019; An et al., 2021; Cunha et al., 2020; Wang et al., 2018). On the other hand, constrained borehole data can accurately access the depth location of faults. The evaluation of the advanced logging techniques can be biased due to local heterogeneities and also interpreters' eyesight (e.g. Genter et al. 1997). In addition, borehole data provide a rather punctual information covering a portion of typically less than 10^{-9} of the target volume (Pyrcz and White, 2015).

With the structural information from seismic or borehole data

* Corresponding author.
E-mail address: Ali.dashti@kit.edu (A. Dashti).

resulting in a conceptual model, hydraulic field tests will further visualize the underground setting. Tracer test, designed in the early 1900s, by itself is a well-documented technology (Cao et al., 2020; Horne and Rodriguez, 1983; Leibundgut and Seibert, 2011) and applied for hydraulic characterization in both the porous and fractured media. Tracer test curves quantify the rate and direction of flow but are unable to provide unique solutions for the location and geometry of faults that control the flow regime.

Wellmann and Regenauer-Lieb (2012) highlighted that lack of data, measurement errors, external disturbances, human factors lead to a ubiquitous uncertainty in geological models. Today, it is highly recommended to include uncertainty estimations in the engineering of underground applications (Caers, 2011; Stamm et al., 2019; Wellmann et al., 2010; Yin et al., 2020).

Given the possible scale of uncertainties, from pore space to the basin structural scale, this study investigates the structural uncertainty rather than sensitivity analyses or addressing specific material sets existing on a once elaborated mesh. To encapsulate the uncertainty, values of the measured properties should be represented as probability distributions.

Typically structural uncertainties are evaluated through attributing different material properties i.e. so called material uncertainty in numerical schemes. Reconstructing geological features e.g. faults and contact of layers is a time consuming and computationally demanding process. The open-source, Python-based implicit modeling package called Gempy (la Varga et al., 2019) is used to generate probabilistic structural models. Herein we establish a novel and fast workflow in Python ecosystem that includes this structural uncertainty directly in the meshing procedure. Developed Python library is called *GeoMeshPy* and converts Gempy outputs into inputs for the mesh generator called GMSH (Geuzaine and Remacle, 2009).

This study aims at assessing the uncertainty of structural information using synthetic tracer test data. The presented numerical scheme should lead to an optimum experimental tracer test design that allows for defining test duration or required tracer mass. The structural uncertainty is included in designing the field tracer experiments and its effect on flow and transport properties is quantified. The manuscript first elaborates the probabilistic setting of the numerical scheme using 50 geological realizations to cover a range of structural possibilities in a hydraulic solute (HS) modeling framework. Then, we quantify how these variations can affect both the tracer test design and interpretations derived from this test.

2. Methodology

2.1. Overall approach

Tracer experiments are resulting in breakthrough curves (BTCs) typically monitored from borehole locations. There are different analytical or numerical models to assess the BTC with different degree of sophistication matching the complexities of geological models (Erol et al., 2022; Li et al., 2021). Available analytical solutions are unable to provide reliable information for underground setting due to simplifications. In inversion scheme of such methods, characteristics like flow condition and dispersion coefficients are tuned in a way to fit a continuous BTCs on sparse measured data (Toride et al., 1993; van Genuchten et al., 2012). They converge to matches without including the possible 3D geometry of the underground.

From the numerical modeling perspective, usually a deterministic geological realization is constructed and parameters are again tuned to fit the field data to results. It is highly time consuming to generate several structural models and later mesh each one. Therefore, the gap between geological models and numerical solvers hampers including structural uncertainty in numerical simulation. Here, we present an automated pipeline to construct these meshes, providing still a large complexity of geological information. Gempy, as the modeling tool, is connected to the mesh generator, GMSH, to create meshes based on the variating structural model. Developed package, *GeoMeshPy*, is able to handle a variety of existing functionalities in Gempy. Available examples[1] can visualize capacities of the developed package. Therefore, 50 different structural realizations with their unique geometries are meshed and fed into the simulator. Each model is discretized based on its geological features e.g. layers and faults before being fed into numerical solver. BTCs are simulated for several perturbed geological realizations with fixed small-scale parameters e.g. porosity, permeability, diffusion and dispersion coefficients, and so on. In the next step, generated BTCs are assessed analytically to quantify the effect of the structural uncertainty on extracted parameters. Then, extracted parameters are compared to the input data of simulations regarding the structural model. Completing this loop can help to quantify the effect of structural uncertainty on the flow characters of underground. The following bullet points summarize the general scheme of this study:

- Generating 50 different structural realizations
- Converting outputs of geomodelling tool into useable inputs for the mesh generator
- Meshing each realization based on its geometry
- Simulating tracer test for each realization with fixed operational input parameters
- Inverting a bandwidth of analytically calculated outputs from simulation results

2.2. Conceptual model

In this study, a generic doublet system is designed to investigate impacts of structural uncertainty on flow-related parameters. The overall scheme of the model follows Soultz-sous-Forêts reservoir which is one of the most well-known Enhanced Geothermal Systems (EGS) (Gérard et al., 2006). Presented doublet system inherits the basic parameters of the mentioned EGS but with less geological complexity. Several authors (Dezayes et al., 2010; Egert et al., 2020; Held et al., 2014; Hooijkaas et al., 2006; Karmakar et al., 2016; Kohl and Mégel, 2007; Sausse et al., 2010; Schmittbuhl et al., 2008) discussed details of most probable flow and fracture systems in Soultz-sous-Forêts. In this study, a simplified model of this EGS is utilized to understand the impact of the structural uncertainty rather than providing deterministic and complicated solutions.

The synthetic doublet system includes two deviated wells (injection and production) penetrating a granite reservoir. Stratigraphically, the geological model contains two different layers: sedimentary cap rock and granitic reservoir. Three faults are also embedded in the doublet system (Fig. 1). Two major big faults called injection and production faults are detected through drilled wells and seismic data. These two faults are abbreviated as Fault_Inj and Fault_Pro-in Fig. 1. The third one, called connecting fault (abbreviated as Fault_Con in Fig. 1), is only observed in seismic data making the geological model uncertain. There are 50 green lines in this figure representing a 2D view of the connecting fault in the middle of the model. Each green line makes a unique geological realization. The geological model includes two certain (!) faults (Fault_Inj and Fault_Pro) cut by wells and the uncertain Fault_Con. The central point of this uncertain fault can modulate in a 60 m depth window to cover a range of possibilities.

Fig. 1 also includes a stereonet showing the considered uncertainty for this connecting fault under the stress field of Soultz. The dipping angle of this fault can vary up to $\pm 15^{\circ}$ Purely unbiased random numbers are generated to perturb the orientation and dipping angle of this connecting fault. Regarding the high uncertainty of seismic data for connecting fault, a surface with zero dip and strike angles ($000^{\circ}/00^{\circ}$) is chosen as the starting point and later perturbed. As the outcome, probabilistic geological models are generated to be fed into numerical

[1] https://github.com/Ali1990dashti/GeoMeshPy/tree/main/Examples

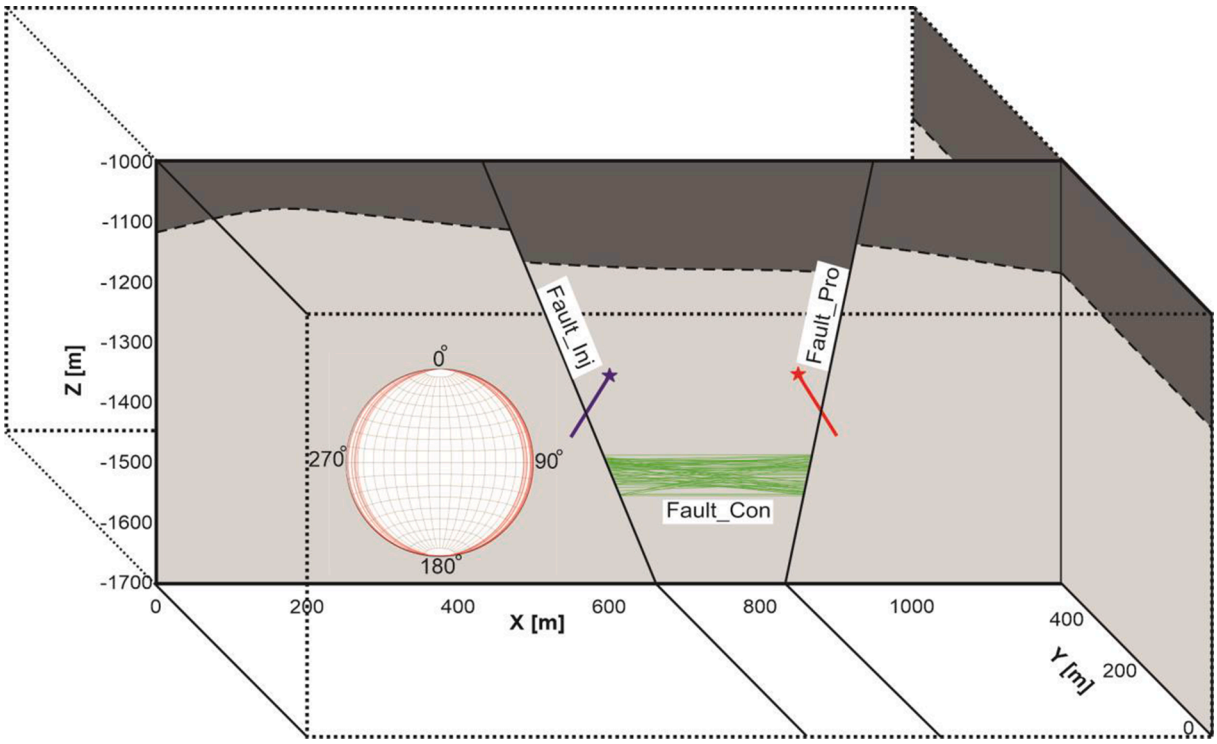

Fig. 1. A 3D schematic view on the synthetic model and designed doublet system. Injection fault (Fault_Inj) is cut by the injection well and production fault (Fault_Pro) is cut by the production well. These two certain faults are shown as continuous black lines and thinner green lines show the trace of the uncertain connecting fault (Fault_Con) in the middle (y 500) of the model. Each green trace is making a unique geological realization. A stereonet showing the different traces of the uncertain connecting fault is also embedded in the figure. Dipping values varying up to ±15° (For interpretation of the references to color in this figure legend, the reader is referred to the web version of this article).

solvers rather than sticking to one single deterministic model. Extension of the model in x, y and z directions is 1200, 1000 and 700 m, respectively.

2.3. Modelling

2.3.1. Geological modeling and vertice conversion

In this study, Gempy, an open source code developed in Python ecosystem, is used for probabilistic geological modeling. The code is highly efficient in generating and visualizing probabilistic structural models based on the potential-field interpolation method (La Varga et al., 2019). As inputs, Gempy requires depth points and orientation of the included features (layers and faults) in the model. The model is then discretized based on the 3-D matrices of lithology and/or fault IDs (Figs. 2 and 3 in Schaaf et al. 2020). As output, it gives vertices representing all the existing features. Gempy uses the potential-field method for interpolations in which faults are unable to cut contacts of formations.

In this study, vertices of one contact of layers and three faults are separated and later refined to be used as inputs for the mesh generator. Contact of layers separates the Granite reservoir from the cap rock. Initially, as a data cleanup step, the redundant points in the vicinity of existing cutting faults i.e. Fault_Inj and Fault_Pro-and contact of formations are removed. Then, the remaining points will be clustered into three groups based on their relationship with two cutting faults. Fig. 2-a shows how Fault_Inj and Fault_Pro-can divide vertices of the layers' contact into three patches.

There are three main issues regarding outputs of the Gempy that *GeoMeshPy* solves. Firstly, vertices have some redundant points. Areas A-I, A-II and A-III are annotated on the Fig. 2-a to highlight these extra points. After removing these redundancies, the remaining vertices will make a regular grid. *GeoMeshPy* can regularize the vertices of as many as exiting layers in the model. Secondly, the contact of the layers is stretched over two cutting faults (areas annotated with B in Fig. 2-a). In order to make vertices applicable for later surfaces generation in GMSH, it is necessary to remove extra points of the existing faults. This way, the countinuous output of Gempy will split into three patches (colorful circles in the figure). After removing the extra points, some new regular points are added to the refined ones in order to make sure that the vertices will pass through fault surfaces. Hollow colorful circle in Fig. 2-a are obviously passing through two cutting faults while the generated geometry in Gempy is also preserved. Then, it is possible to fit a surface to each patch separately. Thirdly, in the case of connecting fault (Fault_Con), Gempy gives the vertices in all over the domain (visualized by letter C in Fig. 2-a). This fault is not making any offset but may have effects on the flow. Therefore, its contact points with two other faults are detected in *GeoMeshPy* to recreate the small red surface of Fig. 2-a in GMSH.

Fig. 2-b shows the final spatial discretization for one of the geological realizations. Besides maintaining the geometry of the model, the mesh generation is accomplished automatically in Python ecosystem. Vertices of Gempy are processed in *GeoMeshPy* and later fed into Python API of the GMSH. Manual mesh generation for 50 geological realizations is a highly time demanding and error-prone process.

2.3.2. Mesh generation

Mesh generation is the primary step in any discretization method applied to solve a physical phenomenon numerically (Ho-Le, 1988). Amongst the commercial and open-source packages that can generate suitable meshes for geological modeling (Okereke and Keates, 2018), the open-source GMSH (Geuzaine and Remacle, 2009) is selected because of its high efficiency, integrated geometrical modeler, and Python API. GMSH has been adopted specifically to create geometrical surfaces passing through an arbitrary set of points, and to intersect them with other CAD entities. Coupled with its ability to generate adapted meshes on non-manifold geometries, this allows to generate conformal meshes

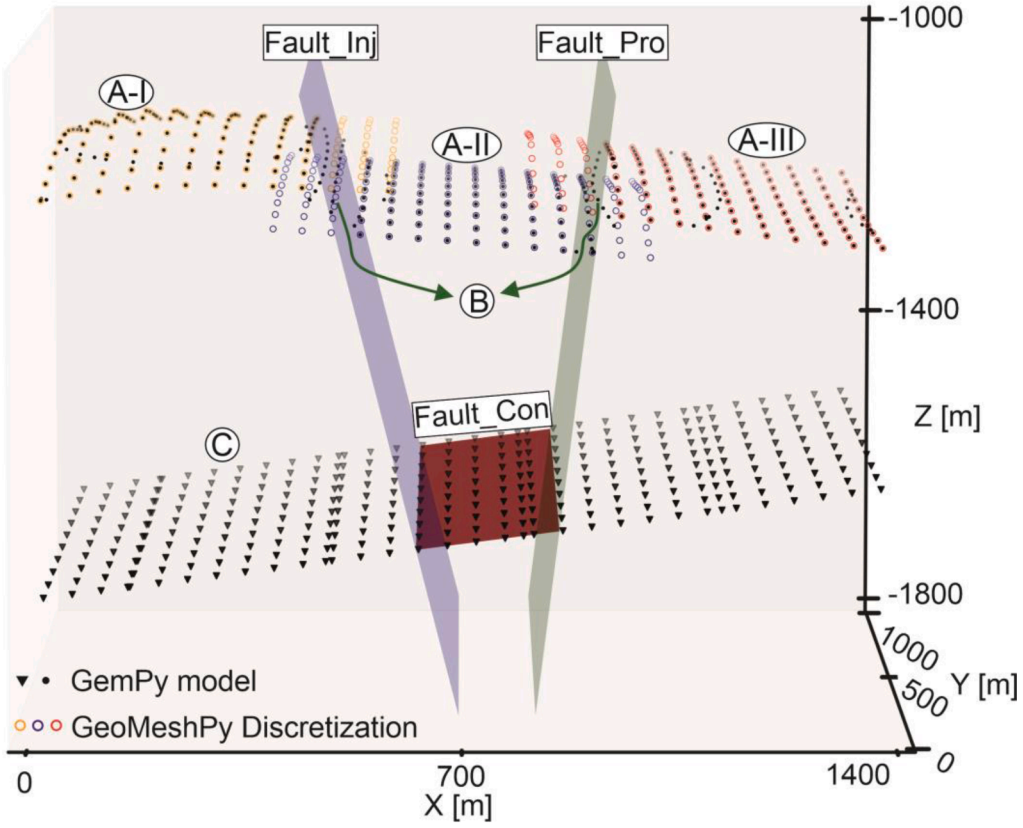

b)

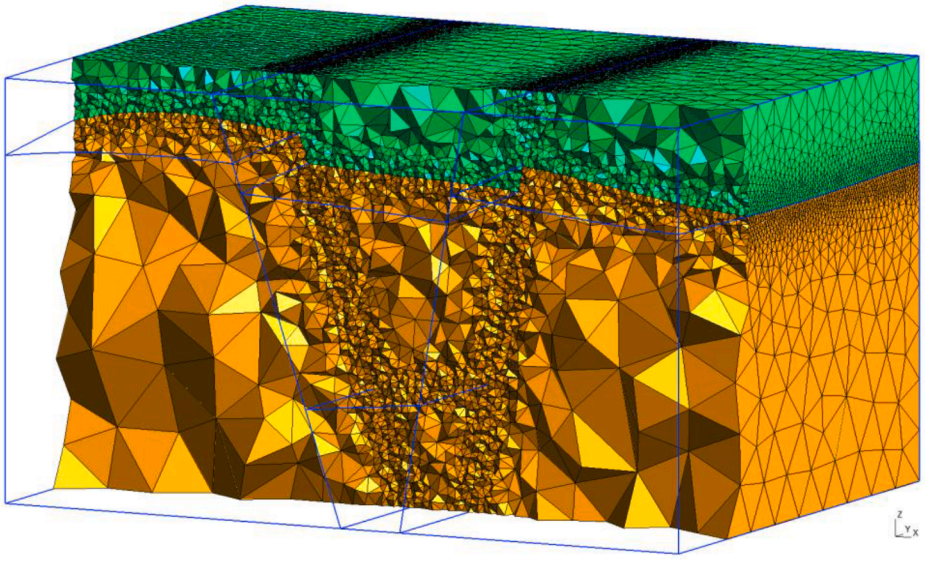

Fig. 2. a- Raw output of Gempy for the contact of layers and connecting fault (Fault_Con) is shown as black dots and triangles, respectively. Colorful circles (orange, blue and red) represent refined vertices separated into three patches in GeoMeshPy. Fault_Inj and Fault_Pro-cut the only exiting contact of layers. The raw output of Gempy has also some redundancies that make the grid irregular in area A-I, A-II and A-III. Area B also shows the continuity of the contact of layers on two faults. GeoMeshPy also reduces the larger Gempy output for the Fault_Con. Contacts of this fault with two other big ones is detected. The red surfaces is made using four calculated corners of connecting fault. b- The generated mesh includes two volumes representing the geological layers (Granite and cap rock) and three faults (For interpretation of the references to color in this figure legend, the reader is referred to the web version of this article).

that can directly inherit geometries from an advanced modeler like Gempy.

In this study outputs of Gempy are modified using *GeoMeshPy* and then imported into GMSH. Fig. 2-b visualizes a cross section of the discretized scheme achieved in GMSH. The new surface fitting functionality in GMSH can be also used for vertices coming from any other geomodelling tool. It only requires a regular grid of vertices and also the indices where vertices should be separated. For example, in the presented case study vertices of the layers' contact is divided into three patches. Therefore, two separation points should be defined for GMSH. Otherwise, there is no other way for the software to distinguish each patch. For more details please see the available examples.[2]

Thanks to the robust and versatile mesh refinement functionality[3] in GMSH, after recreating all the geological features, the mesh size is automatically refined in the vicinity of important features (Fig. 2-b).

2.3.3. *Numerical simulation*

An open source finite element (FE) application called TIGER

[2] https://github.com/Ali1990dashti/GeoMeshPy/tree/main/Examples
[3] https://gmsh.info/doc/texinfo/gmsh.html#Specifying-mesh-element-sizes

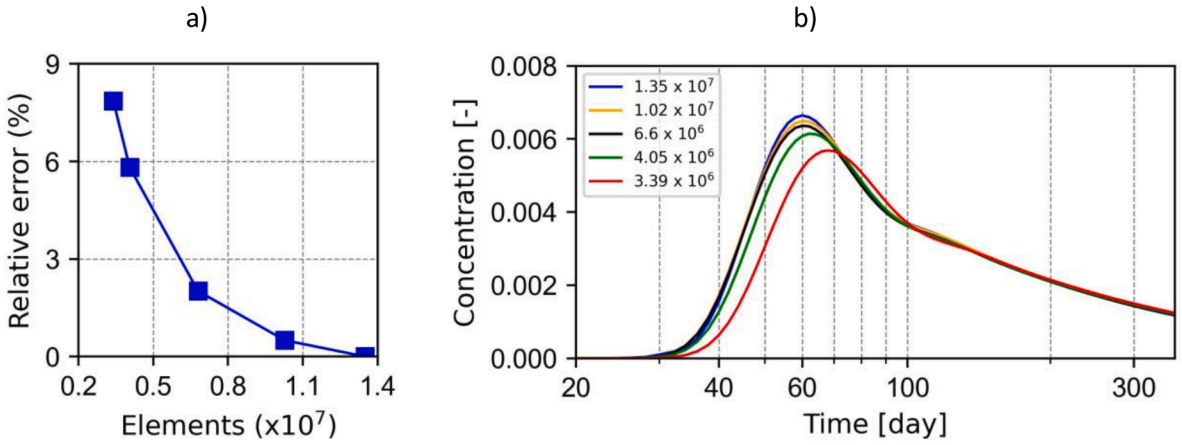

Fig. 3. (a) The relative error in tracer retrieval peak values versus the number of elements. (b) Corresponding BTCs of each mesh. After the required level of refinement (6.6×10^6 elements), BTCs are almost similar.

(Thermo-Hydro-Chemical simulator for Geoscience Research) (Gholami Korzani et al., 2020) is used to simulate a tracer test. TIGER is developed on the top of MOOSE (Multiphysics Object-Oriented Simulation Environment) framework (Gaston et al., 2009; Tonks et al., 2012). MOOSE is a fully implicit coupled FE toolkit inherits all the capabilities of PETSc (a suite of data structures and routines for the scalable parallel solution of scientific application) and libMesh libraries. Inheriting from the state-of-the-art FE solver, TIGER can quantify Thermo-Hydro-Chemical processes in geothermal domains (Gholami Korzani et al., 2020). TIGER solves the hydraulic field of the pore pressure by combining mass and momentum balances including Darcy's law. Details of the TIGER's mathematical background are addressed in Gholami Korzani et al. (2020). With TIGER the user have access to most of available solvers and preconditioning schemes. In this study Newton based nonlinear solver that uses a basic line search is used as the nonlinear solver. Hypre's algebraic multigrid (AMG) package (BoomerAMG) is selected as the linear preconditioner. Hypre is a set of solvers/preconditioners from Lawrence Livermore National Laboratory. PETSc[4] and MOOSE[5] documentations elaborated mathematical backgrounds of the selected solvers. In this study the problem is solved fully implicitly in the TIGER. Streamline upwinding schemes of MOOSE were used to simulate model regions of high advection (Brooks and Hughes, 1982; Masud and Hughes, 2002).

In TIGER, fractures can be considered as lower-dimensional elements, which leads to a mixed-dimensional problem formulation. The important note is that lower dimensional elements should be properly connected using embedment functionality of GMSH with higher dimensional ones. Otherwise, isolated elements will be unable to be coupled with higher ones. For example, fluid i.e. tracer is unable to flow from an isolated well represented by 1D lines toward faults (2D surfaces) or matrix (3D volume).

Tracer transport natural phenomena is also solved based on advection-diffusion-dispersion equations. Both space and time changes are included in hydraulic kernel of TIGER:

$$\frac{\varphi \partial C}{\partial t} + (\quad \nabla . D_m \nabla C + q \nabla . C) = Q \tag{1}$$

where φ represents the porosity; C is the solute concentration; t is time; D_m is sum of molecular diffusion and dispersion, q is the darcy velocity and Q is the source/sink term for injection/production of tracer. Required mathematical details of the tracer transport equations are discussed in literature (Egert et al., 2020; Gholami Korzani et al., 2020).

Table 1 represents the parametrization used for all the simulations of the tracer test.

3. Results and discussion

3.1. Mesh sensitivity analysis

To investigate numerical results dependency with respect to spatial discretization, different customized refinements are applied. Field option in GMSH is an efficient functionality allowing for refining meshes close to points, lines or surfaces while gradually coarsening from a given distance.[6] This way, many adequately fine elements will be generated in a user-defined area around important parts of the model. In tracer transport modeling, 1D wellbores and 2D faults are controlling factors due to high hydraulic and tracer gradients variations. Accordingly, connection of faults and wellbores with 3D elements has been considered as another influential point of the model.

Regarding these remarks, defining proper mesh sizes is challenging and results revealed that mesh size on fault surfaces plays the most important role. Hence, different mesh sizes on fault surfaces were tried and Fig. 3-a shows the relative error versus the number of elements in one of the realizations. The independent solution was achieved when mesh size is 0.25 m around the wells (the radius of < 3 m) and it is 5 m

Table 1
Parameters selected to design a generic tracer test. Data origin is marked a to show it is considered in this study, b, c and d are coming from Egert et al. (2020), Kestin et al. (1981) and Zhou et al. (2007), respectively.

Parameters		Values
Flow rate [l s^{-1}]	Injection	45 [a]
	Production	45 [a]
Permeability [m^2]	Matrix (reservoir)	1.0×10^{-16} [b]
Porosity [-]	Faults	1 [a]
	Matrix (reservoir)	0.05 [a]
Aperture [m]	Injection Fault	0.2 [b]
	Production Fault	0.15 [b]
	Connecting Fault	0.5 [b]
Transmissivity [m^2 s^{-1}] at 25°C	Injection Fault	1.2×10^{-6} [a]
	Production Fault	3.3×10^{-7} [a]
	Connecting Fault	5.6×10^{-7} [a]
Faults' dispersion coefficients [m]	Longitudinal	15 [d]
	Transverse	5 [d]
Solute diffusion [m^2 s^{-1}]		4.0×10^{-10} [c]
Simulation time [day]		366 [a]

[4] https://petsc4py.readthedocs.io/en/stable/
[5] https://mooseframework.inl.gov/
[6] https://gmsh.info/doc/texinfo/gmsh.html#Specifying-mesh-element-sizes

on the fault surfaces (up to 25 m away from the fault surfaces). Total number of elements in this mesh is 1.35×10^7. However, a coarser mesh with less elements (6.6×10^6 versus 1.35×10^7) was used which has about 2% relative error. This reduction in number of elements can save more than 90 min for the computation time running on 24 cores of a High Performance Computing cluster. The difference between meshes with 1.02×10^7 and 1.35×10^7 is also negligible, i.e. less than 0.5%. Therefore, it is decided to choose the required refinement level having 6.6×10^6 elements. Fig. 3-b also represents the BTCs of each mesh. As the figure shows, the mesh with 6.6×10^6 yields enough accuracy and the difference with finer meshes is negligible.

3.2. Tracer flow simulations

To quantify impacts of structural uncertainty, 50 different geological realizations are designed to simulate a tracer test experiment with the same hydraulic and tracer parameters (Table 1). The tracer is injected 24 h during day 8 while the response is monitored for a one-year period in the production well. Fig. 4 shows BTCs plotted in a logarithmic time scale and peak concentration values marked with red crosses. The peak arrival time varies between day 54 and 68. Two weeks delay in arrival time, as well as a 30% reduction in peaks magnitude, are clear shreds of evidence to highlight the importance of structural uncertainty that can influence expectations from such an important field test.

In the simulations the produced fluid at the production well is reinjected to the injection well. Therefore, the circulating fluid has concentrations of the tracer for the duration of the simulation even after the day 9 when the tracer injection stopped. The observed second peaks between days 100 and 150 of simulation in Fig. 4 are caused by this reinjection rather than multiple flow paths or stagnation zones. Approaching the end of simulation time, all BTCs are converging toward similar values while the reinjection again causes the difference. For example, the difference of BTCs in the day 300 is far less than day 60. After the second peak no further rises are observed. This can be interpreted as the low concentrations of tracers are fading out due to dispersion and diffusion rather than advective transport within the fault networks.

The pressure field is also another important factor, especially in geothermal applications. Flow rate and underground structures mainly control the pressure field. Fig. 5 shows the evolution of the pore pressure field in both injection (blue) and production (red) wells. As shown in the figure, compared to solute concentration the pore pressure is less sensitive to structural uncertainty. But, it can be clearly seen that the connecting fault still affects the pore pressure field, particularly at the production well. The pressure drop at the production well is varying about 8% while at injection well it is less than 1.2%. The difference in the aperture and permeability of faults makes this evolution curve asymmetric. Production fault has less aperture and permeability compared to injection fault (Table 1) that make the pressure drop more severe than the pressure rise. Transmissivity variations of three faults caused such pressure fields in injection and production wells.

3.3. Controlling mechanisms of the tracer concentration

In the designed model, tracer is passing through three different conduits (the injection, connecting and production faults) and also the matrix. It is usually assumed that each medium contributes to the flow based on its transmissivity. For example, three conductive faults are mainly moving the tracer from injection toward production point through advection. Meanwhile, tracer diffusion into the almost impermeable matrix can increase the long-term concentration results but with a lowered peak. Fig. 6 visualizes the idea of sequential multi-flow features deployed in this study. The figure shows the tracer distribution on the day 54 of tracer injection for the maximum peak realization. Tracer transport within faults area is mainly advection dominated while it diffuses into the surrounding matrix. Therefore, both the small and structural scale properties of main conduits (three faults) are controlling the tracer movement. As this figure shows, tracer plume moves from the injection point toward the production. Beside the internal properties of the faults, their structural impact on the tracer plume is investigated in the following.

Annotations on Fig. 6 provide a schematic view of the designed structural model in order to demonstrate some possibly controlling geometrical elements of the model. Connections of the wells and the certain (as explained before) injection and production faults are fixed for all 50 realizations. Two filled stars represent where the injection and the connecting faults (P1) and also the production and the connecting faults (P2) meet each other. Accordingly, different pathway lengths, names on the as L_{Inj}, L_{Con} and L_{Pro} stem from changes in the location of the connecting fault. In the figure, wells are extended in the x-z plane in the middle of the model ($y = 500$ m), and L_{Inj}, L_{Con} and L_{Pro} are also measured on the same plane. This figure demonstrates one realization (out of 50) where the connecting fault dips upward from the injection well toward the production well and the depth of the P1 is higher than P2. In contrast, downward dipping is when the connecting fault intersects the production fault deeper than the injection fault, i.e. the P1 will be shallower than P2. In case of having depth difference less than 10 m between two points (P1 and P2), the connecting fault can be assumed as a horizontal plane.

The length of the connecting fault (L_{Con}) is expected to be a

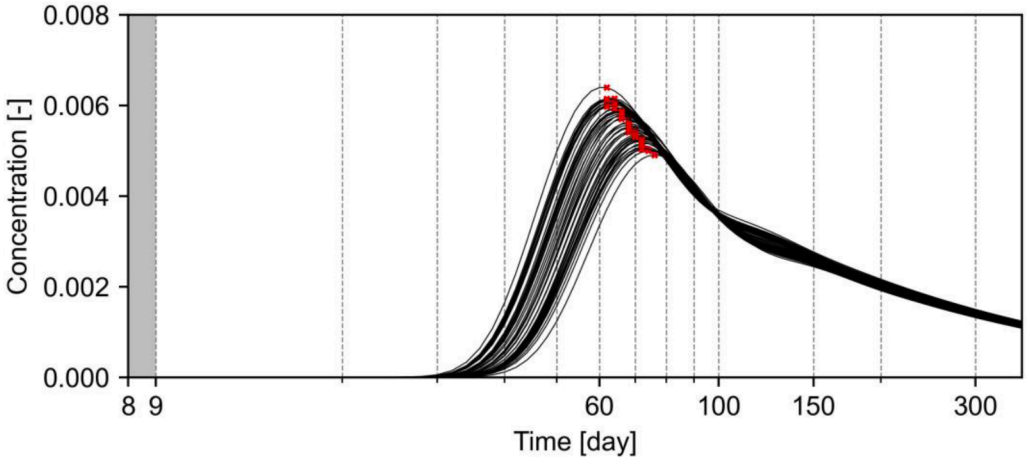

Fig. 4. Extracted solute concentration at the production well for 50 different geological realizations. Values for tracer concentration are unitelss and tracer is injected with concentration 1 in day 8 (greyed out).

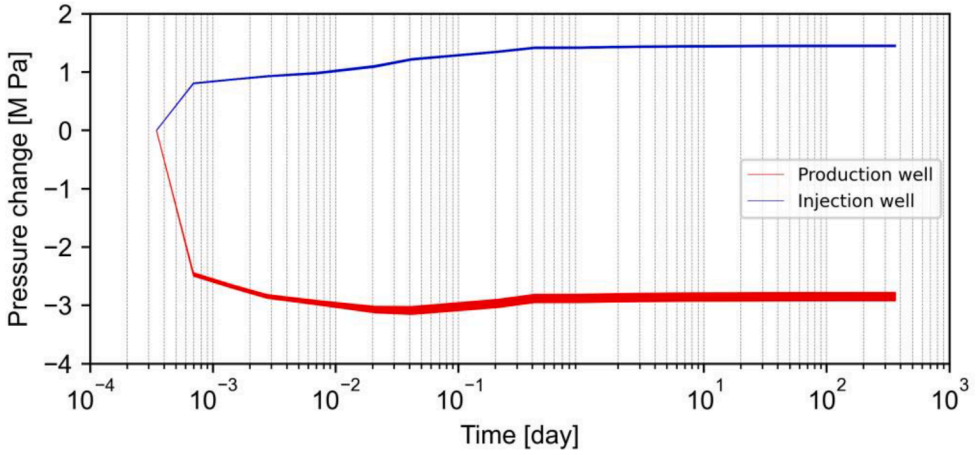

Fig. 5. Pressure changes during one year of 45 l/s injection and production for 50 different geological realizations.

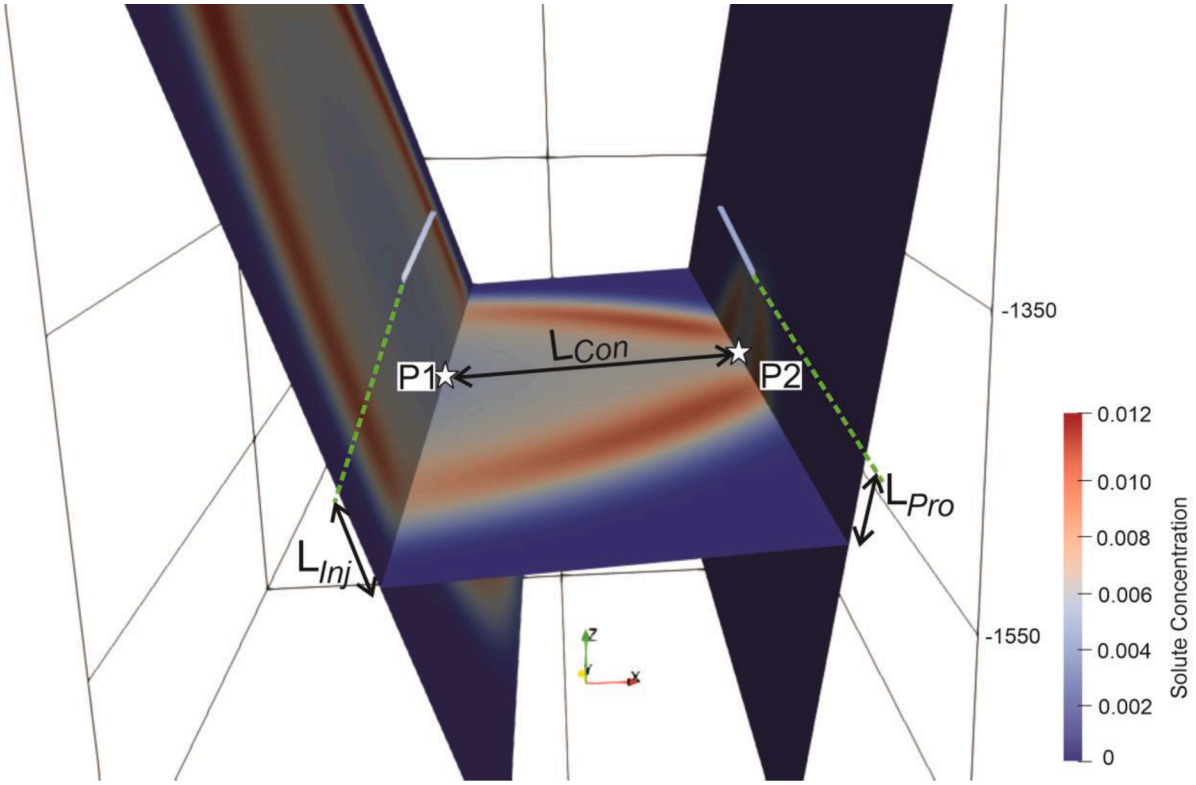

Fig. 6. The concentration of the tracer in the peak time (day 54) of the realization with the highest concentrations magnitude. Tracer plume is observable as a red ring. The most important geometrical parameters are annotated. The length of injection (L_{Inj}) measures the distance from the connection of the injection well and fault to the intersection of injection and connecting faults (P1). The length of production (L_{Pro}) represents the distance from the connection of the production well and fault to the intersection of production and connecting faults (P2). The length of connection (L_{Con}) is the length of the connecting faults intersected with the other two faults (For interpretation of the references to color in this figure legend, the reader is referred to the web version of this article).

controlling geometry. Fig. 7 shows L_{Con} and the total length ($L_{Inj} + L_{Con} + L_{Pro}$) versus normalized (based on the median) peak values of all 50 realizations. Surprisingly, Fig. 7-a demonstrates a direct relationship between the peak concentration values and the length of the connecting fault due to the overall structure of the model. As shown in Fig. 6, ignoring the dipping angle, if the connecting fault goes deeper, its length decreases but the total pathway for tracer transport will be longer and deeper. Because of the model's geometry, less L_{Con} results in higher total lengths. In the case of the total length (Fig. 7-b), the concentration decrease by increasing the length (a reverse relationship).

To further investigate impacts of the connecting faults, all peaks are marked based on the dipping angles of the connecting fault. It is clearly observable in Fig. 7-a that upward dipping realizations resulted in higher peak values . This trend suggests that length of production (L_{Pro}) should be investigated because when the connecting fault is dipping upward, L_{Pro} decreases. Additionally, these upward realizations (and horizontal ones) show a very good linear relationship. As the next step, the impact of total length of the flow path is investigated in Fig. 7-b. The total lengths in most of upward realizations are shorter than the median length as its marker signs (crosses) in Fig. 7-b are mainly clustered in the left-hand side of the scatter plot. The best linear correlation is found in the realizations with almost horizontal dipping as expected. The

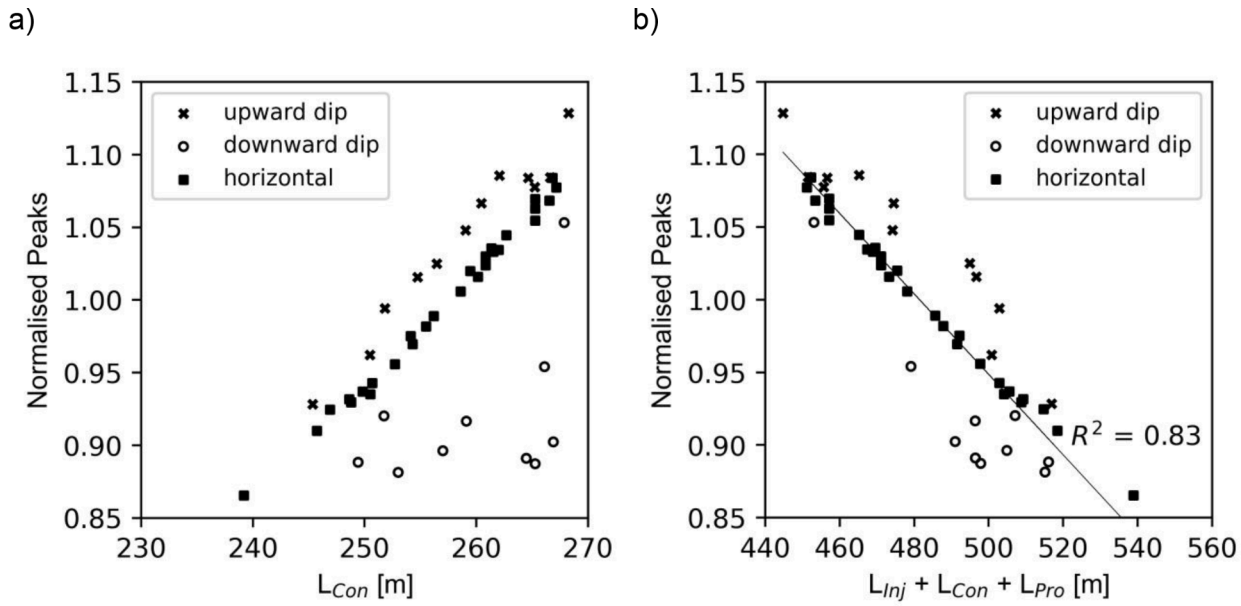

Fig. 7. a- Normalized peak concentration values plotted versus the connecting fault lengths. b- Normalized peak concentration values plotted versus the total length of the pathways.

relatively weak linear correlation ($R^2 = 0.83$) necessitates finding more influential parameters on tracer concentration.

Fig. 8-a visualizes the normalized peak concentrations versus the production length (L_{Pro}, refer to Fig. 6). This figure is colored and clustered based on the recorded peak arrival times. The first clear conclusion is that the less the L_{Pro}, the higher the peak and the earlier the recorded time. Secondly, the correlation has increased and reached a reasonable value (R^2 equals 0.95). L_{Pro} can be considered as the most sensitive geometry factor . In fact, the dipping angle of the connecting faults is playing a major role because it can control both the total length of the pathway and also length of production.

However, there are still 5% mismatch between L_{Pro} prediction and simulation results. For example, the green dots cluster representing BTCs which their peaks recorded on the day 60 are highly scattered. Minor impact of other two distances (L_{Inj} and L_{Con}) can cause such complexity in different realizations. Fig. 8-b shows cross-sections of the highly scattered (green) and concentrated (orange) clusters. This figure also includes two realizations with the maximum (red line) and the minimum (blue) peak of tracer concentration. In the green cluster, the angle and the direction of the connecting fault are highly diverse while in the orange cluster the connecting faults are almost horizontal. As expected, dipping angle variations modify both the total length and L_{Pro} that is detected to be a leading parameter. The correlation coefficient can get closer to 1 by excluding the green cluster. This cluster highlights the fact that only one single parameter (L_{Pro}) is unable to predict the tracer peak values with 100% accuracy. Several geometrical parameters are superposed on each other to make such flow regime and tracer recovery.

3.4. *Tracer tests design and data inversion*

In tracer campaigns, operators usually wait for a predefined amount of time to detect the concentrations of injected tracer. But, a small structural perturbation in the underground can have unexpected impacts on detection time and concentration. Ignoring uncertainty and unrealistic expectations can result in an early shut down of tests and considering conduits as barrier zones. In reverse, an obscure connecting fault can be misrepresented as an efficient conduit, i.e. a structural bias leads to overestimations for the flow. However, a computationally affordable uncertainty analysis can avoid such hazardous and expensive failures.

BTCs characterize the flow regime (Becker and Shapiro, 2000, 2003), and are usually analyzed based on the first detection and the arrival peak time of the tracer concentration in a production well. Tailing in BTCs indicates the presence of stagnation zones. Peak arrival time provides information to calculate the transmissivity of the main flow conduit. Furthermore, longitudinal and transversal dispersion coefficients are estimated based on the time difference of the initial arrival and peak times and bandwidth of the peak. To extract the mentioned information, an inversion process is required where BTCs are usually fitted to measured concentration values based on velocity, length of flow paths, dispersion coefficients and so on. A myriad of analytical methods are proposed in the literature (Bodin, 2020; Tenebe et al., 2016; van Genuchten et al., 2012) to carry out inversion.

Fig. 9 shows two simulated BTCs (out of 50) in this study and their corresponding fitted curves using the Multi-Flow Inversion of Tracer (MFIT) tool (Bodin, 2020). The Single-Fracture Dispersion Model (SFDM) (Maloszewski and Zuber, 1990) module of MFIT enabling solute transport as advection-dispersion in fractures and diffusion in the matrix, is applied to make these fits. BTCs with the highest and lowest peaks are deliberately selected as the most critical simulations. For both BTCs, the difference between fitted curves and data points is effortlessly observable. The second mode of tracer concentrations (between days 100 to 150) is missing in both fitted curves. Apart from peak magnitudes, the other difference is in the initial arrival time. As discussed in detail, the effect of dip direction in conjunction with the geometry in different realizations controls the flow. However, fitted curves are proposing faster initial arrival times due to ignoring the complexity of the flow path as available analytical approaches miss it.

On the other hand, dispersion coefficients can be simply considered as the standard deviation of a BTC (Hauns et al., 2001). Fitted curves are proposing higher standard deviations due to their early initial arrival times. The smaller peak magnitudes of the fits can also reveal that dispersion coefficients are exaggerated in the analytical solver. After day 170 of simulation, two fitted curves converge toward exactly the same values. This means that the analytical solver considered diffusion as the only process transferring the tracer after this time. However, the absolute values of the tail in the fitted curves are less than the half of the simulated BTCs due to overestimating the diffusion. It is noteworthy that the area below each BTC is equal to its corresponding fitted curve.

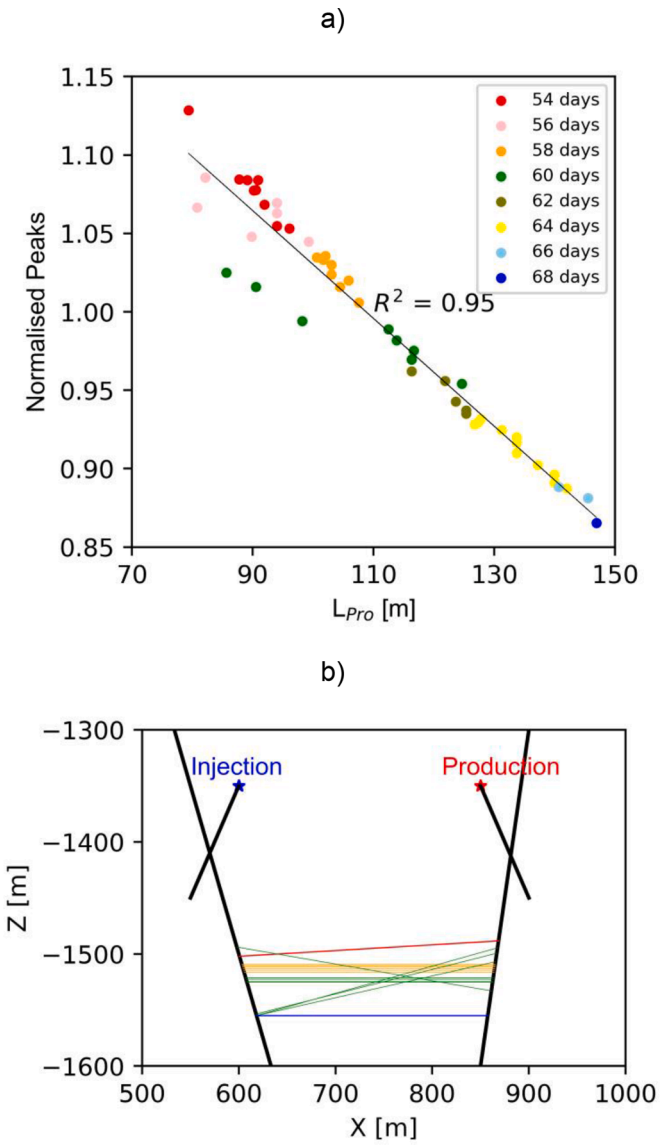

Fig. 8. a- Normalized peak concentration values plotted versus the length of the connection in the production fault and colored by the peak arrival times. b- Green lines represent the realizations where the connecting fault orientation is highly scattered (day 60). Orange lines represent the realizations where the connecting fault orientation is the most concentrated (day 58). Red and blue lines also represent the realizations with the highest and lowest peak concentrations, respectively (For interpretation of the references to color in this figure legend, the reader is referred to the web version of this article).

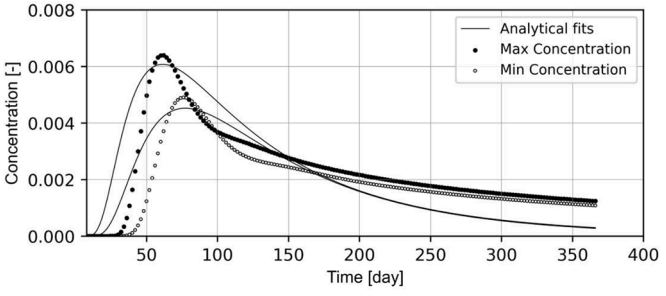

Fig. 9. Realizations with the highest and lowest peak magnitudes are shown as black dots and circles, respectively. Their corresponding fitted analytical solutions are represented as continuous black lines.

Providing reliable characteristics of the complicated pathways using analytical approaches can be cumbersome. Mathematically, several curves can be fitted to a bunch of points. Physically, obtaining and measuring coefficients and flow parameters (dispersion coefficients or Péclet number Huysmans and Dassargues 2005) can be error-prone. For example, two fitted curves in Fig. 9 have different Péclet numbers that are set to be 3.4 and 4.3 for fitted curves of maximum and minimum peak concentration BTCs, respectively. The total distance parameter ($L_{Inj} + L_{Con} + L_{Pro}$) is the reason behind the different Péclet numbers in these two realizations. The different distances arise from structural uncertainty that is often ignored. The following equation correlates Péclet number (Pe) with dispersion coefficient:

$$Pe = \frac{u\,L}{D_L} \tag{1}$$

Where, u [m s ^{1}] is velocity, L [m] is total distance ($L_{Inj} + L_{Con} + L_{Pro}$) in flow direction and D_L [m^2 s ^{1}] represents longitudinal hydrodynamic dispersion coefficient for fracture network (Zhao et al., 2010). In this study, molecular diffusion is assumed to be negligible (solute diffusion equals 4.0 $\times$ 10 ^{10} m^2 s ^{1} in Table 1). Longitudinal hydrodynamic dispersion coefficient is calculated using:

$$D_L = u\,a_L \tag{2}$$

where a_L [m] is the longitudinal dispersion coefficient. Combining Eqs. (1) and (2) results in:

$$Pe = \frac{L}{a_L} \tag{3}$$

Routinely, it is assumed that the total length of the pathway (L: $L_{Inj} + L_{Con} + L_{Pro}$) is known i.e. fixed. But length can have a major role in changing the Péclet number. Ignoring L of the maximum and minimum realizations resulted in overestimation of dispersion coefficients in the maximum realization. The analytically calculated longitudinal dispersion coefficients (using Eq. (3)) of minimum and maximum peak realizations are 125.6 and 129.4 m, respectively. These two numbers are much higher than the used value in the simulations (15 m as per Table 1). The high dispersivity of the fitted curves stems from ignoring the complicated flow direction from injection toward production well. Higher dispersion of the maximum realization is also due to its lower Péclet number (3.4). Fitted curves propose different Péclet numbers and dispersion coefficients that is caused by structural geology (L) rather material properties (a_L). However, these analytically calculated variables are unable to reflect the existing uncertainty in the geological model.

4. Conclusion

In this study an application of the new tool, *GeoMeshPy* is described on the example of a tracer injection in a fractured system. *GeoMeshPy* is at the interface between GemPy and GMSH allowing to automate the generation of customized meshes accounting for well-refined geological structures. This tool can transfer the structural uncertainty of GemPy into a numerical mesh. In parallel, GMSH, has been updated with the new functionality to automatically emulate structures created in geomodelling tools.

The case study was selected carefully to quantify the impact of probabilistic geometries on tracer breakthrough curves, BTCs, in multi-fractured systems. These BTCs represent a typical setting for underground structures explored by doublet borehole systems. Our *GeoMeshPy* based simulations demonstrate that BTCs are strongly affected when varying the orientation of a connecting fault, assumed as a key structural element in the geological model. In contrast to parametric sensitivity analyses, our models were fully remeshed to represent the real geological uncertainty with the highest possible numerical accuracy. The stochastic procedure allowed to attribute a key importance to

the length of the production well (L_{Pro}). The generated, 50 geometries – following a normal distribution – are affecting the length of the total flow circulation, either by shortening or extending. Assuming fixed operational parameters, the pressure values also fluctuated due to variations of the structural model. Both, the arrival peak time and concentration magnitude are affected by the introduced uncertainty. Realizations, in which the connecting fault dips upward toward the production, yield BTCs with higher tracer peak concentrations and earlier arrival times due to its shorter pathway on the production fault.

In a next step, the numerically simulated BTCs were inverted for estimating the overall dispersion coefficient, based on standard analytical methods. It is shown that such analytic calculation schemes are unable to reproduce realistic dispersion coefficients as well as the applied structural setting. The calculated coefficients are considerably higher than the simulated values by as much as one order of magnitude. This overestimation is caused by ignoring the complex flow path through sequentially connected fractures. Even the rather simple model setting applied here may pose an unsolvable puzzle for analytical solvers.

The possibilities of applying *GeoMeshPy* in future are abundant. Although being applied herein in a synthetic case study on BTC, future applications will result in quantifying the geomertrical uncertainty for different real concepts like nuclear waste disposal or storage. Furthermore, such structural uncertainty analyses allows to design field tests like time schedule and required mass of tracer.

CRediT authorship contribution statement

Ali Dashti: Conceptualization; Methodology; Simulation; Validation; Code development; Writing– original draft & editing
Maziar Gholami Korzani: Methodology; Supervision; Code development; Writing – review & editing
Christophe Geuzaine: Code development; Writing – review & editing
Robert Egert: Code development
Thomas Kohl: Conceptualization; Supervision; Writing – review & editing.

Code availability

GeoMeshPy is a free, open-source Python library licensed under the MIT License. It is hosted on the GitHub repository https://github.com/Ali1990dashti/GeoMeshPy. The package is also available as a standard python package (https://pypi.org/project/geomeshconv/).

Declaration of Competing Interest

The authors declare that they have no known competing financial interests or personal relationships that could have appeared to influence the work reported in this paper.

Acknowledgments

Ali Dashti is receiving the financial support from The German Academic Exchange Service (Deutscher Akademischer Austauschdienst: DAAD) to do his PhD in Germany as the Research Grants- Doctoral programmes in Germany 2019/20. This organization is appreciated for giving the opportunity to researchers. The study is also part of the Helmholtz portfolio project Geoenergy. The support from the program “Renewable Energies", under the topic “Geothermal Energy Systems”, is gratefully acknowledged. Dr. Jacques Bodin is appreciated due to his help on using MFIT and informative comments.

References

Al-Khdheeawi, E.A., Vialle, S., Barifcani, A., Sarmadivaleh, M., Iglauer, S., 2017. Impact of reservoir wettability and heterogeneity on CO_2 -plume migration and trapping capacity. Int. J. Greenh. Gas Control 58, 142–158.

Al-Maskeen, A.A., Ali, S.S., Khan, M., 2019. The impact of automated fault detection and extraction technology on seismic interpretation, in: day 2 Tue, March 19, 2019. SPE Middle East Oil and Gas Show and Conference, Manama, Bahrain. 3/18/2019 - 3/ 21/2019. SPE.

An, Y., Guo, J., Ye, Q., Childs, C., Walsh, J., Dong, R., 2021. Deep convolutional neural network for automatic fault recognition from 3D seismic datasets. Comput. Geosci. 153, 104776.

Becker, M.W., Shapiro, A.M., 2000. Tracer transport in fractured crystalline rock: evidence of nondiffusive breakthrough tailing. Water Resour. Res. 36 (7), 1677–1686.

Becker, M.W., Shapiro, A.M., 2003. Interpreting tracer breakthrough tailing from different forced-gradient tracer experiment configurations in fractured bedrock. Water Resour. Res. 39 (1).

Bodin, J., 2020. MFIT 1.0.0: multi-flow inversion of tracer breakthrough curves in fractured and karst aquifers. Geosci. Model Dev. 13 (6), 2905–2924.

Brooks, A.N., Hughes, T.J., 1982. Streamline upwind/Petrov-Galerkin formulations for convection dominated flows with particular emphasis on the incompressible Navier- Stokes equations. Comput. Methods Appl. Mech. Eng. 32 (1–3), 199–259.

Caers, J., 2011. Modeling Uncertainty in the Earth Sciences. John Wiley & Sons, Ltd, Chichester, UK.

Cao, C., Xu, Z., Chai, J., Li, Y., 2019. Radial fluid flow regime in a single fracture under high hydraulic pressure during shear process. J. Hydrol. 579, 124142 (Amst). Cao, V., Schaffer, M., Taherdangkoo, R., Licha, T., 2020. Solute reactive tracers for hydrogeological applications: a short review and future prospects. Water 12 (3), 653 (Basel).

Cox, S.F., 2020. Chapter 2: the dynamics of permeability enhancement and fluid flow in overpressured, fracture-controlled hydrothermal systems, in: Rowland, J.V., Rhys, D. A. (Eds.), Applied Structural Geology of Ore-forming Hydrothermal Systems. Society of Economic Geologists, pp. 25–82.

Cunha, A., Pochet, A., Lopes, H., Gattass, M., 2020. Seismic fault detection in real data using transfer learning from a convolutional neural network pre-trained with synthetic seismic data. Comput. Geosci. 135, 104344.

Dezayes, C., Genter, A., Valley, B., 2010. Structure of the low permeable naturally fractured geothermal reservoir at Soultz. C.R. Geosci. 342 (7–8), 517–530.

Egert, R., Korzani, M.G., Held, S., Kohl, T., 2020. Implications on large-scale flow of the fractured EGS reservoir Soultz inferred from hydraulic data and tracer experiments. Geothermics 84, 101749.

Egert, R., Nitschke, F., Gholami Korzani, M., Kohl, T., 2021. Stochastic 3D navier-stokes flow in self-affine fracture geometries controlled by anisotropy and channeling. Geophys. Res. Lett. 48 (9).

Erol, S., Bayer, P., Akın, T., Akın, S., 2022. Advanced workflow for multi-well tracer test analysis in a geothermal reservoir. Geothermics 101, 102375.

Fairley, J.P., Hinds, J.J., 2004. Rapid transport pathways for geothermal fluids in an active Great Basin fault zone. Geol 32 (9), 825.

Faleide, T.S., Braathen, A., Lecomte, I., Mulrooney, M.J., Midtkandal, I., Bugge, A.J., Planke, S., 2021. Impacts of seismic resolution on fault interpretation: insights from seismic modelling. Tectonophysics 816, 229008.

Fauziah, C.A., Al-Khdheeawi, E.A., Iglauer, S., Barifcani, A., 2020. Effect of clay minerals heterogeneity on wettability measurements: implications for CO_2 storage. In: Proceedings of the Offshore Technology Conference Asia. OTC, 11/2/2020 - 11/6/2020.

Flohr, A., Matter, J.M., James, R.H., Saw, K., Brown, R., Gros, J., Flude, S., Day, C., Peel, K., Connelly, D., Pearce, C.R., Strong, J.A., Lichtschlag, A., Hillegonds, D.J., Ballentine, C.J., Tyne, R.L., 2021. Utility of natural and artificial geochemical tracers for leakage monitoring and quantification during an offshore controlled CO_2 release experiment. Int. J. Greenh. Gas Control 111, 103421.

Gaston, D., Newman, C., Hansen, G., Lebrun-Grandié, D., 2009. MOOSE: a parallel computational framework for coupled systems of nonlinear equations. Nucl. Eng. Des. 239 (10), 1768–1778.

Genter, A., Castaing, C., Dezayes, C., Tenzer, H., Traineau, H., Villemin, T., 1997. Comparative analysis of direct (core) and indirect (borehole imaging tools) collection of fracture data in the Hot Dry Rock Soultz reservoir (France). J. Geophys. Res. 102 (B7), 15419–15431.

Gérard, A., Genter, A., Kohl, T., Lutz, P., Rose, P., Rummel, F., 2006. The deep EGS (Enhanced Geothermal System) project at Soultz-sous-Forêts (Alsace, France). Geothermics 35 (5–6), 473–483.

Geuzaine, C., Remacle, J.F., 2009. Gmsh: a 3-D finite element mesh generator with built-in pre- and post-processing facilities. Int. J. Numer. Meth. Eng. 79 (11), 1309–1331.

Gholami Korzani, M., Held, S., Kohl, T., 2020. Numerical based filtering concept for feasibility evaluation and reservoir performance enhancement of hydrothermal doublet systems. J. Pet. Sci. Eng. 190, 106803.

Hadgu, T., Karra, S., Kalinina, E., Makedonska, N., Hyman, J.D., Klise, K., Viswanathan, H.S., Wang, Y., 2017. A comparative study of discrete fracture network and equivalent continuum models for simulating flow and transport in the far field of a hypothetical nuclear waste repository in crystalline host rock. J. Hydrol. 553, 59–70 (Amst).

Hauns, M., Jeannin, P.Y., Atteia, O., 2001. Dispersion, retardation and scale effect in tracer breakthrough curves in karst conduits. J. Hydrol. 241 (3–4), 177–193 (Amst).

Held, S., Genter, A., Kohl, T., Kölbel, T., Sausse, J., Schoenball, M., 2014. Economic evaluation of geothermal reservoir performance through modeling the complexity of the operating EGS in Soultz-sous-Forêts. Geothermics 51, 270–280.

Ho-Le, K., 1988. Finite element mesh generation methods: a review and classification. Comput. Aided Des. 20 (1), 27–38.
Hooijkaas, G.R., Genter, A., Dezayes, C., 2006. Deep-seated geology of the granite intrusions at the Soultz EGS site based on data from 5km-deep boreholes. Geothermics 35 (5–6), 484–506.
Horne, R.N., Rodriguez, F., 1983. Dispersion in tracer flow in fractured geothermal systems. Geophys. Res. Lett. 10 (4), 289–292.
Huysmans, M., Dassargues, A., 2005. Review of the use of Péclet numbers to determine the relative importance of advection and diffusion in low permeability environments. Hydrogeol. J. 13 (5–6), 895–904.
Jenkins, C., Chadwick, A., Hovorka, S.D., 2015. The state of the art in monitoring and verification—ten years on. Int. J. Greenh. Gas Control 40, 312–349.
Karmakar, S., Ghergut, J., Sauter, M., 2016. Early-flowback tracer signals for fracture characterization in an EGS developed in deep crystalline and sedimentary formations: a parametric study. Geothermics 63, 242–252.
Kestin, J., Khalifa, E., Correia, R., 1981. Tables of the dynamic and kinematic viscosity of aqueous NaCl solutions in the temperature range 20–150 C and the pressure range 0.1–35 MPa. J. Phys. Chem. Ref. Data.
Klein, E., Hardie, S.M.L., Kickmaier, W., McKinley, I.G., 2021. Testing repository safety assessment models for deep geological disposal using legacy contaminated sites. Sci. Total Environ. 776, 145949.
Kohl, T., Mégel, T., 2007. Predictive modeling of reservoir response to hydraulic stimulations at the European EGS site Soultz-sous-Forêts. Int. J. Rock Mech. Min. Sci. 44 (8), 1118–1131.
Konrad, F., Savvatis, A., Degen, D., Wellmann, F., Einsiedl, F., Zosseder, K., 2021. Productivity enhancement of geothermal wells through fault zones: efficient numerical evaluation of a parameter space for the Upper Jurassic aquifer of the North Alpine Foreland Basin. Geothermics 95, 102119.
Varga, La, de, M., Schaaf, A., Wellmann, F., 2019. GemPy 1.0: open-source stochastic geological modeling and inversion. Geosci. Model Dev. 12 (1), 1–32. Leibundgut, C., Seibert, J., 2011. Tracer hydrology. Treatise on Water Science. Elsevier, pp. 215–236.
Li, L., Jiang, H., Wu, K., Li, J., Chen, Z., 2019. An analysis of tracer flowback profiles to reduce uncertainty in fracture-network geometries. J. Pet. Sci. Eng. 173, 246–257.
Li, X., Wen, Z., Zhan, H., Wu, F., Zhu, Q., 2021. Laboratory observations for two-dimensional solute transport in an aquifer-aquitard system. Environ. Sci. Pollut. Res. Int. 28 (29), 38664–38678.
Lu, J., Cook, P.J., Hosseini, S.A., Yang, C., Romanak, K.D., Zhang, T., Freifeld, B.M., Smyth, R.C., Zeng, H., Hovorka, S.D., 2012. Complex fluid flow revealed by monitoring CO 2 injection in a fluvial formation. J. Geophys. Res. 117 (B3).
Malik, D., Abidin, Z., Pramono, B., 2020. Tritium tracer Injection test at Wayang Windu Geothermal Field, West Java, Indonesia. Geothermics 83, 101718.
Maloszewski, P., Zuber, A., 1990. Mathematical modeling of tracer behavior in short-term experiments in fissured rocks. Water Resour. Res. 26 (7), 1517–1528.
Masud, A., Hughes, T.J., 2002. A stabilized mixed finite element method for Darcy flow.
Comput. Methods Appl. Mech. Eng. 191 (39–40), 4341–4370.
Michie, E.A.H., Mulrooney, M.J., Braathen, A., 2021. Fault interpretation uncertainties using seismic data, and the effects on fault seal analysis: a case study from the Horda Platform, with implications for CO₂ storage.
Middleton, R.S., Carey, J.W., Currier, R.P., Hyman, J.D., Kang, Q., Karra, S., Jiménez-Martínez, J., Porter, M.L., Viswanathan, H.S., 2015. Shale gas and non-aqueous fracturing fluids: opportunities and challenges for supercritical CO2. Appl. Energy 147, 500–509.
Okereke, M., Keates, S., 2018. Finite element mesh generation. In: Okereke, M., Keates, S. (Eds.), Finite Element Applications. Springer Tracts in Mechanical Engineering. Springer International Publishing, Cham, pp. 165–186.
Phillips, T., Kampman, N., Bisdom, K., Forbes Inskip, N.D., Hartog, S.A.D., Cnudde, V., Busch, A., 2020. Controls on the intrinsic flow properties of mudrock fractures: a review of their importance in subsurface storage. Earth Sci. Rev. 211, 103390. Pyrcz, M.J., White, C.D., 2015. Uncertainty in reservoir modeling. Interpretation 3 (2), SQ7–SQ19.
Røe, P., Georgsen, F., Abrahamsen, P., 2014. An uncertainty model for fault shape and location. Math. Geosci. 46 (8), 957–969.
Sanjuan, B., Pinault, J.L., Rose, P., Gérard, A., Brach, M., Braibant, G., Crouzet, C., Foucher, J.C., Gautier, A., Touzelet, S., 2006. Tracer testing of the geothermal heat exchanger at Soultz-sous-Forêts (France) between 2000 and 2005. Geothermics 35 (5–6), 622–653.
Sausse, J., Dezayes, C., Dorbath, L., Genter, A., Place, J., 2010. 3D model of fracture zones at Soultz-sous-Forêts based on geological data, image logs, induced microseismicity and vertical seismic profiles. C.R. Geosci. 342 (7-8), 531–545. Schaaf, A., La Varga, M.D., Wellmann, F., Bond, C.E., 2020. Constraining stochastic 3-D structural geological models with topology information using approximate Bayesian computation using GemPy 2.1.
Schmittbuhl, J., Steyer, A., Jouniaux, L., Toussaint, R., 2008. Fracture morphology and viscous transport. Int. J. Rock Mech. Min. Sci. 45 (3), 422–430.
Siler, D.L., Pepin, J.D., 2021. 3-D Geologic Controls of Hydrothermal Fluid Flow at Brady geothermal field, Nevada, USA. Geothermics 94, 102112.
Stamm, F.A., Varga, La, de, M., Wellmann, F., 2019. Actors, actions, and uncertainties: optimizing decision-making based on 3-D structural geological models. Solid Earth 10 (6), 2015–2043.
Tenebe, I.T., Ogbiye, A.S., Omole, D.O., Emenike, P.C., 2016. Estimation of longitudinal dispersion co-efficient: a review. Cogent Eng. 3 (1), 1216244.
Tonks, M.R., Gaston, D., Millett, P.C., Andrs, D., Talbot, P., 2012. An object-oriented finite element framework for multiphysics phase field simulations. Comput. Mater. Sci. 51 (1), 20–29.
Toride, N., Leij, F.J., van Genuchten, M.T., 1993. A comprehensive set of analytical solutions for nonequilibrium solute transport with first-order decay and zero-order production. Water Resour. Res. 29 (7), 2167–2182.
Tsang, Y.W., Tsang, C.F., Hale, F.V., Dverstorp, B., 1996. Tracer transport in a stochastic continuum model of fractured media. Water Resour. Res. 32 (10), 3077–3092.
van Genuchten, M.T., Å imunek, J, Leij, F.J, Toride, N., Å ejna, M., 2012. STANMOD: model use, calibration, and validation. Trans. ASABE 55 (4), 1355–1368.
Wang, Z., Di, H., Shafiq, M.A., Alaudah, Y., AlRegib, G., 2018. Successful leveraging of image processing and machine learning in seismic structural interpretation: a review. Lead. Edge 37 (6), 451–461.
Wellmann, J.F., Horowitz, F.G., Schill, E., Regenauer-Lieb, K., 2010. Towards incorporating uncertainty of structural data in 3D geological inversion. Tectonophysics 490 (3–4), 141–151.
Wellmann, J.F., Regenauer-Lieb, K., 2012. Uncertainties have a meaning: information entropy as a quality measure for 3-D geological models. Tectonophysics 526-529, 207–216.
Yin, Z., Strebelle, S., Caers, J., 2020. Automated Monte Carlo-based quantification and updating of geological uncertainty with borehole data (AutoBEL v1.0). Geosci. Model. Dev. 13 (2), 651–672.
Zhang, Q., Luo, S., Ma, H., Wang, X., Qian, J., 2019. Simulation on the water flow affected by the shape and density of roughness elements in a single rough fracture. J. lHydrol. 573, 456–468 (Amst).
Zhao, Z., Jing, L., Neretnieks, I., 2010. Evaluation of hydrodynamic dispersion parameters in fractured rocks. J. Rock Mech. Geotech. Eng. 2 (3), 243–254.
Zhou, Q., Liu, H.H., Molz, F.J., Zhang, Y., Bodvarsson, G.S., 2007. Field-scale effective matrix diffusion coefficient for fractured rock: results from literature survey. J. Contam. Hydrol. 93 (1–4), 161–187.